AIAA JOURNAL
Vol. 43, No. 7, July 2005

Three-Dimensional Thermomechanical Buckling of Functionally Graded Materials

Kyung-Su Na* and Ji-Hwan Kim†
Seoul National University, Seoul 151-742, Republic of Korea

Three-dimensional thermomechanical buckling analysis is discussed for functionally graded materials. Material properties are varied continuously in the thickness direction according to a simple power-law distribution. The three-dimensional finite element model is adopted using an 18-node solid element and the assumed-strain mixed formulation is used to prevent locking as well as to maintain kinematic stability for thin structures. The thermal buckling behavior under time-dependent temperature rise is compared with that under time-independent temperature rise. In time-dependent temperature distribution, temperature at each node is obtained by solving the thermomechanical equations and the Crank–Nicolson method is used for a time discretization. In the case of time-independent temperature distribution, thermal buckling is investigated under uniform, linear, and sinusoidal temperature rise. Numerical results are compared with those of previous works. In addition, the changes of critical buckling temperature due to temperature field, volume fraction distributions, and system geometric parameters are studied.

Nomenclature

a	=	length of plate
b	=	width of plate
$\boldsymbol{E}$	=	assumed strain vector
$\boldsymbol{E}^0$	=	initial strain vector
$\bar{\boldsymbol{E}}$	=	displacement-dependent strain vector
h	=	thickness of plate
n	=	volume fraction index
$\boldsymbol{P}$	=	assumed strain polynomial matrix
$\boldsymbol{q}$	=	nodal displacement vector
$\boldsymbol{S}$	=	second Piola–Kirchhoff stress vector
T	=	temperature field
t	=	time
u, v, w	=	displacements in x, y, and z directions, respectively
V_m, V_c	=	volume fraction of metal and ceramic
α	=	thermal expansion coefficient
$\boldsymbol{\beta}$	=	assumed strain parameter vector

I. Introduction

FUNCTIONALLY graded materials (FGMs) are composites that have spatially varying composition designed to take advantage of the attractive features of each of their constituents. Generally a ceramic and a metal constitute an FGM. From the continuous change in composition of these materials, FGMs can withstand high-temperature environments while maintaining their structural integrity. Because of these advantages, FGMs have been researched and applied in many engineering parts.

Markworth et al.[1] described the modeling studies relative to FGMs. They included two aspects of the modeling procedure: models for microstructure-dependent thermophysical properties, and models for the design, processing, and performance of FGMs. Ravichandran[2] presented a one-dimensional calculation of thermal stresses arising from the fabrication of an FGM system. The residual stresses were found to increase when fully ceramic and/or fully metal regions were included in the structure, adjoining the graded zone. Fuchiyama and Noda[3] developed computer programs that analyzed the transient heat transfer and the transient thermal stress of an FGM plate, composed of ZrO_2 and Ti–6Al–4V, by the finite element method. Reddy and Cheng[4] studied three-dimensional thermomechanical deformations of a simply supported Monel®–zirconia functionally graded rectangular plate by using an asymptotic method. The locally effective material properties were estimated by the Mori–Tanaka scheme. Cheng and Batra[5] obtained a new solution in closed form for the thermomechanical deformations of an isotropic linear thermoelastic functionally graded elliptic plate rigidly clamped at the edges. The through-thickness variation of the volume fraction of the ceramic phase in a metal–ceramic plate was assumed to be given by a power-law-type function. The effective material properties at a point were computed by the Mori–Tanaka scheme. Vel and Batra[6] presented an analytical solution for three-dimensional thermomechanical deformations of a simply supported FGM plate subjected to time-dependent thermal loads on its top or bottom surfaces. The temperature, displacements, and stresses at critical locations for transient thermal loads were investigated. Cho and Oden[7] analyzed thermal-stress characteristics of FGM beams using the Crank–Nicolson–Galerkin scheme. The effects of the material variation through the thickness and the size of the FGM layer inserted between ceramic (Al_2O_3) and metal (Ni) layers were studied using the finite element method. Feldman and Aboudi[8] studied the elastic bifurcational buckling of an Al–SiC FGM plate under in-plane compressive loading. To analyze the problem, a method based on a combination of micromechanical and structural approaches was employed. Javaheri and Eslami[9] derived the equilibrium and stability equations of a functionally graded rectangular plate under thermal loads, based on the classical plate theory. Buckling analysis of FGM plates under four types of thermal loads was carried out in closed-form solutions. Najafizadeh and Eslami[10] discussed the thermal buckling of an FGM circular plate. The nonlinear equilibrium and linear stability equations were derived using variational formulations. The critical temperatures were derived for simply supported and clamped edges. Yang and Shen[11] presented the nonlinear bending analysis of shear deformable FGM plates subjected to thermomechanical loads and under various boundary conditions. Theoretical formulations were based on Reddy's higher order shear deformation plate theory and included the thermal effects due to temperature rise. A seminumerical approach was employed to calculate the nonlinear bending of the plates. Lanhe[12] derived the equilibrium and stability equations of a thick FGM plate under thermal loads based on the first-order shear deformation theory. The critical

Received 23 February 2004; revision received 4 February 2005; accepted for publication 6 February 2005.

*Research Assistant, School of Mechanical and Aerospace Engineering, San 56-1, Shinrim-Dong, Kwanak-Ku.

†Professor, School of Mechanical and Aerospace Engineering, San 56-1, Shinrim-Dong, Kwanak-Ku. Member AIAA.

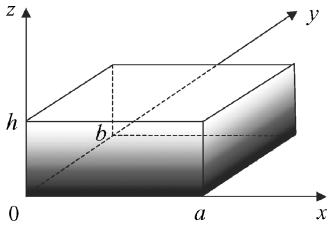

Fig. 1 Geometry of a functionally graded rectangular plate.

temperatures under uniform and gradient temperature rise through the thickness direction were obtained. Na and Kim[13] studied the three-dimensional thermal buckling analysis of FGM plates using the finite element method. In this, an 18-node solid element and the assumed-strain mixed formulation were applied. The thermal buckling behavior under uniform or nonuniform temperature rise was analyzed; however, the time-dependent temperature rise was not considered.

In this work, we investigate the thermal buckling analysis of FGMs using the finite element method. For more accurate modeling of material properties and temperature field in the thickness direction, a three-dimensional solid element is used. Furthermore, an assumed-strain mixed formulation is adopted to prevent locking as well as to maintain kinematic stability for thin structures. Material properties are varied continuously in the thickness direction according to a simple power-law distribution. The thermal buckling behavior under time-dependent temperature rise is compared with that under time-independent temperature rise. In time-dependent temperature distribution, temperature at each node is obtained by solving the thermomechanical equations and, for a time discretization, the Crank–Nicolson method is used. In the case of time-independent temperature distribution, the temperature field is assumed uniform, linear, and sinusoidal through the thickness direction. To check the validity of the numerical results, the critical temperatures of isotropic plates and the temperature field of an FGM composite beam are compared with those of previous works. In addition, the thermal buckling behavior of FGMs due to temperature field, volume fraction distributions, and system geometric parameters are investigated.

II. Modeling of FGMs

A ceramic–metal FGM rectangular plate is represented in Fig. 1. Material properties are assumed to be varied in the z direction only, and the dark and bright regions correspond to metal and ceramic particles, respectively. On the top surface ($z = h$), the plate is composed entirely of ceramic and is graded to the bottom surface ($z = 0$), which is composed entirely of metal. The volume fractions of metal, V_m, and ceramic, V_c, are expressed as follows by applying a simple power-law distribution:

$$V_m(z) = (1 - z/h)^n, \qquad V_c(z) = 1 - V_m(z) \tag{1}$$

where volume fraction index n indicates the material variation profile through the thickness direction and is a nonnegative real number.

According to the linear rule of mixtures, the effective material properties P_{eff} can be obtained as follows:

$$P_{\text{eff}}(z) = P_m V_m(z) + P_c V_c(z) = P_c + (P_m - P_c)(1 - z/h)^n \tag{2}$$

where P_m and P_c are material properties of the metal and ceramic, respectively.

III. Finite Element Discretization

A three-dimensional finite element model for thin and thick FGM plates is developed. An 18-node solid element is selected to more accurately analyze the variation of material properties and temperature field in the thickness direction of the structure. In addition, the assumed-strain mixed formulation is adopted to prevent locking as well as to maintain kinematic stability for thin plates.[13,14]

A. Thermomechanical Equations

In the case of FGM plates under time-dependent temperature distribution, the temperature at each node is obtained by solving the thermomechanical equations and, for a time discretization, the Crank–Nicolson method is used.

The general heat conduction equation can be expressed as[7]

$$\rho c \frac{\partial T}{\partial t} - \nabla \cdot (k \nabla T) = \frac{\partial q}{\partial t} \tag{3}$$

where ρ, c, k, and q indicate the density, specific heat, thermal conductivity, and internal heat source, respectively.

The Dirichlet boundary condition is defined as

$$T(x, y) = T_S|_{S=S_1} \tag{4}$$

where x and y denote the position on the surface S_1, and T_s is an initially specified temperature field. The Neumann boundary conditions are defined as

$$k \nabla T \cdot \boldsymbol{n} = q_B|_{S=S_2}, \qquad k \nabla T \cdot \boldsymbol{n} = h(T - T_c)|_{S=S_3} \tag{5}$$

where S_2 and S_3 denote the surfaces acted on by the external convective and radiative fluxes, respectively. The temperature field T in Eq. (3) can be expressed in terms of element nodal temperatures T_e as follows:

$$T = \boldsymbol{N}\boldsymbol{T}_e, \qquad \dot{T} = \boldsymbol{N}\dot{\boldsymbol{T}}_e \tag{6}$$

where $\boldsymbol{N}$ indicates the shape function matrix. The following equation is obtained by multiplying Eq. (3) by $\boldsymbol{N}^T$ and integrating analytically in element levels:

$$\sum_e \int \boldsymbol{N}^T \left[\rho c \frac{\partial T}{\partial t} - \nabla \cdot (k \nabla T) \right] \mathrm{d}V_e = \sum_e \int \boldsymbol{N}^T \frac{\partial q}{\partial t} \, \mathrm{d}V_e \tag{7}$$

where the notation $\sum$ with subscript e stands for summation over elements and the variables with subscript e indicate the elemental quantities. By applying Green's theorem, Eq. (7) can be expressed as

$$\sum_e \left[\int \boldsymbol{N}^T \rho c \frac{\partial T}{\partial t} \, \mathrm{d}V_e + \int \nabla \boldsymbol{N}^T \cdot (k \nabla T) \, \mathrm{d}V_e + \int_{S_3} h(T - T_c) \, \mathrm{d}S_e \right]$$

$$= \sum_e \left[\int \boldsymbol{N}^T \frac{\partial q}{\partial t} \, \mathrm{d}V_e + \int_{S_2} \boldsymbol{N}^T q_B \, \mathrm{d}S_e \right] \tag{8}$$

Substituting Eq. (6) into Eq. (8), the following equation is obtained[15]:

$$\sum_e \boldsymbol{C}_{Te} \dot{\boldsymbol{T}}_e + \boldsymbol{K}_{Te} \boldsymbol{T}_e = \sum_e \boldsymbol{R}_e \tag{9}$$

where

$$\boldsymbol{C}_{Te} = \int \boldsymbol{N}^T \rho c \boldsymbol{N} \, \mathrm{d}V_e$$

$$\boldsymbol{K}_{Te} = \int \left(\boldsymbol{N}_{,x}^T k_x \boldsymbol{N}_{,x} + \boldsymbol{N}_{,y}^T k_y \boldsymbol{N}_{,y} + \boldsymbol{N}_{,z}^T k_z \boldsymbol{N}_{,z} \right) \mathrm{d}V_e + \int_{S_{qc}} \boldsymbol{N}^T h \boldsymbol{N} \, \mathrm{d}S_e$$

$$\boldsymbol{R}_e = \int \boldsymbol{N}^T \dot{q} \, \mathrm{d}V_e + \int_{S_2} \boldsymbol{N}^T q_B \, \mathrm{d}S_e + \int_{S_3} \boldsymbol{N}^T h T_c \, \mathrm{d}S_e \tag{10}$$

After assembling over all elements, Eq. (9 becomes

$$\boldsymbol{C}_T \dot{\boldsymbol{T}} + \boldsymbol{K}_T \boldsymbol{T} = \boldsymbol{R} \tag{11}$$

For a time discretization, the Crank–Nicolson method is applied.[7,15] Two temperature states, separated by time increment Δt, are denoted by $\boldsymbol{T}_{n+1}$, $\boldsymbol{T}_n$ and they have the following relation:

$$\boldsymbol{T}_{n+1} = \boldsymbol{T}_n + [(1 - \beta)\dot{\boldsymbol{T}}_n + \beta \dot{\boldsymbol{T}}_{n+1}] \Delta t \tag{12}$$

where 0.5 is selected for a value of factor β.[15]

By writing Eq. (11) for times t and $t+\Delta t$, and by multiplying the first equation by $(1-\beta)$ and the second by β, the following equations are obtained:

$$(1-\beta)(\boldsymbol{C}_T\dot{\boldsymbol{T}}_n+\boldsymbol{K}_T\boldsymbol{T}_n)=(1-\beta)\boldsymbol{R}_n$$

$$\beta(\boldsymbol{C}_T\dot{\boldsymbol{T}}_{n+1}+\boldsymbol{K}_T\boldsymbol{T}_{n+1})=\beta\boldsymbol{R}_{n+1} \tag{13}$$

One can obtain the following equation by adding Eqs. (13) and using Eq. (12) to eliminate time derivatives of temperature:

$$[(1/\Delta t)\boldsymbol{C}_T+\beta\boldsymbol{K}_T]\boldsymbol{T}_{n+1}=[(1/\Delta t)\boldsymbol{C}_T-(1-\beta)\boldsymbol{K}_T]\boldsymbol{T}_n$$
$$+(1-\beta)\boldsymbol{R}_n+\beta\boldsymbol{R}_{n+1} \tag{14}$$

From a known $\boldsymbol{T}_0$ at $t=0$ and from Eq. (14), the temperature field at each node can be obtained in each time step.

B. Assumed-Strain Mixed Formulation

To develop an assumed-strain mixed formulation, we consider a three-dimensional solid body in equilibrium[13,14]:

$$\int \delta\bar{\boldsymbol{E}}^T\boldsymbol{S}\,\mathrm{d}V-\delta\boldsymbol{W}=0 \tag{15}$$

where $\delta\bar{\boldsymbol{E}}^T$, $\delta\boldsymbol{W}$, and V indicate the virtual strain vector, external virtual work, and the volume of the undeformed configuration. Introducing an independent assumed strain vector $\boldsymbol{E}$ and an initial strain vector $\boldsymbol{E}^0$ in addition to the displacement-dependent strain vector $\bar{\boldsymbol{E}}$, the compatibility condition is expressed as

$$\int \delta\boldsymbol{S}^T(\bar{\boldsymbol{E}}-\boldsymbol{E}-\boldsymbol{E}^0)\,\mathrm{d}V=0 \tag{16}$$

In a thermal environment, the initial strain vector can be expressed as

$$\boldsymbol{E}^0=[\alpha_x\Delta T\quad \alpha_y\Delta T\quad \alpha_z\Delta T\quad 0\quad 0\quad 0]^T \tag{17}$$

where α are coefficients of thermal expansion in the principal material directions and ΔT is the temperature rise. The independent stress vector $\boldsymbol{S}$ is related to the independent strain vector $\boldsymbol{E}$ through the following equations:

$$\boldsymbol{S}=\boldsymbol{C}\boldsymbol{E} \tag{18}$$

where

$$\boldsymbol{S}=[S_{xx}\quad S_{yy}\quad S_{zz}\quad S_{xy}\quad S_{yz}\quad S_{zx}]^T$$
$$\boldsymbol{E}=[E_{xx}\quad E_{yy}\quad E_{zz}\quad E_{xy}\quad E_{yz}\quad E_{zx}]^T \tag{19}$$

and $\boldsymbol{C}$ is the 6×6 elastic matrix of material stiffnesses, defined in the local coordinate system. Using Eq. (18), the equilibrium and the compatibility condition can be expressed as

$$\int \delta\bar{\boldsymbol{E}}^T\boldsymbol{C}\boldsymbol{E}\,\mathrm{d}V-\delta\boldsymbol{W}=0 \tag{20}$$

$$\int \delta\boldsymbol{E}^T\boldsymbol{C}(\bar{\boldsymbol{E}}-\boldsymbol{E}-\boldsymbol{E}^0)\,\mathrm{d}V=0 \tag{21}$$

The displacement-dependent strain vector $\bar{\boldsymbol{E}}$ and the assumed strain vector $\boldsymbol{E}$ can be expressed as

$$\bar{\boldsymbol{E}}=\boldsymbol{B}\boldsymbol{q} \tag{22}$$

$$\boldsymbol{E}=\boldsymbol{P}\boldsymbol{\beta} \tag{23}$$

where matrix $\boldsymbol{B}$ relates the strain to the nodal displacement vector $\boldsymbol{q}$, $\boldsymbol{P}$ is the assumed strain polynomial matrix, and $\boldsymbol{\beta}$ is the assumed strain parameter vector. The assumed strain field is given in Appendix A.[14] Substituting Eqs. (22) and (23) into Eqs. (20) and (21) and by integrating analytically in element levels, one can obtain the following equations:

$$\sum_e \delta\boldsymbol{q}_e^T\left(\boldsymbol{G}^T\boldsymbol{\beta}-\boldsymbol{Q}_a\right)=0 \tag{24}$$

$$\sum_e \delta\boldsymbol{\beta}^T(\boldsymbol{G}\boldsymbol{q}_e-\boldsymbol{H}\boldsymbol{\beta}-\boldsymbol{G}_0)=0 \tag{25}$$

where

$$\boldsymbol{G}=\int \boldsymbol{P}^T\boldsymbol{C}\boldsymbol{B}\,\mathrm{d}V_e,\qquad \boldsymbol{H}=\int \boldsymbol{P}^T\boldsymbol{C}\boldsymbol{P}\,\mathrm{d}V_e$$

$$\boldsymbol{G}_0=\int \boldsymbol{P}^T\boldsymbol{C}\boldsymbol{E}^0\,\mathrm{d}V_e \tag{26}$$

and the external load vector $\boldsymbol{Q}_a$ is defined as

$$\delta\boldsymbol{W}_e=\delta\boldsymbol{q}_e^T\boldsymbol{Q}_a \tag{27}$$

From Eq. (25), the following equation can be obtained:

$$\boldsymbol{\beta}=\boldsymbol{H}^{-1}\boldsymbol{G}\boldsymbol{q}_e-\boldsymbol{H}^{-1}\boldsymbol{G}_0 \tag{28}$$

which is the discretized compatibility condition at an element level.

Substituting Eq. (28) into Eq. (24),

$$\sum_e \delta\boldsymbol{q}_e^T(\boldsymbol{K}_e\boldsymbol{q}_e-\boldsymbol{Q}_e)=0 \tag{29}$$

where

$$\boldsymbol{K}_e=\boldsymbol{G}^T\boldsymbol{H}^{-1}\boldsymbol{G},\qquad \boldsymbol{Q}_e=\boldsymbol{G}^T\boldsymbol{H}^{-1}\boldsymbol{G}_0+\boldsymbol{Q}_a \tag{30}$$

After assembling over all elements, Eq. (29) becomes

$$\delta\boldsymbol{q}^T(\boldsymbol{K}\boldsymbol{q}-\boldsymbol{Q})=0 \tag{31}$$

where $\boldsymbol{K}$ is the global tangent stiffness matrix and $\boldsymbol{Q}$ is the global nodal load vector. From Eq. (31),

$$\boldsymbol{K}\boldsymbol{q}=\boldsymbol{Q} \tag{32}$$

which can be solved for global nodal displacement vector $\boldsymbol{q}$.

C. Thermal Buckling Analysis

The critical temperature is obtained by solving the following standard eigenvalue problem:

$$(\boldsymbol{K}+\lambda\boldsymbol{K}^b)\boldsymbol{q}^D=0 \tag{33}$$

where λ and $\boldsymbol{q}^D$ are the eigenvalue and the associated mode shape, respectively. In addition, $\boldsymbol{K}^b$ is the stress stiffness matrix, which is obtained by assembling the element geometry matrix $\boldsymbol{K}_e^b$ (Ref. 15):

$$\boldsymbol{K}_e^b=\int \boldsymbol{G}_b^T\boldsymbol{S}_b\boldsymbol{G}_b\,\mathrm{d}V_e \tag{34}$$

where

$$\boldsymbol{S}_b=\begin{bmatrix}\boldsymbol{S}_0 & \boldsymbol{0} & \boldsymbol{0}\\ \boldsymbol{0} & \boldsymbol{S}_0 & \boldsymbol{0}\\ \boldsymbol{0} & \boldsymbol{0} & \boldsymbol{S}_0\end{bmatrix},\qquad \boldsymbol{S}_0=\begin{bmatrix}S_{xx0} & S_{xy0} & S_{zx0}\\ S_{xy0} & S_{yy0} & S_{yz0}\\ S_{zx0} & S_{yz0} & S_{zz0}\end{bmatrix}$$

$$[S_{xx0}\quad S_{yy0}\quad S_{zz0}\quad S_{xy0}\quad S_{yz0}\quad S_{zx0}]^T=-\boldsymbol{C}\boldsymbol{P}\boldsymbol{\beta} \tag{35}$$

and matrix $\boldsymbol{G}_b$ is defined as

$$[u_{,x}\quad u_{,y}\quad u_{,z}\quad v_{,x}\quad v_{,y}\quad v_{,z}\quad w_{,x}\quad w_{,y}\quad w_{,z}]^T=\boldsymbol{G}_b\boldsymbol{q}_e \tag{36}$$

By solving Eq. (33), the critical temperature T_{cr} is obtained as follows:

$$T_{\mathrm{cr}}=T_{\mathrm{ref}}+\Delta T_{\mathrm{cr}}=T_{\mathrm{ref}}+\lambda_{\mathrm{cr}}\Delta T \tag{37}$$

where ΔT_{cr} and λ_{cr} are the critical temperature gradient and the smallest eigenvalue, respectively.

IV. Numerical Results and Discussion

To verify the present study, the critical temperatures under uniform and linear temperature rise are compared with the previous works for the case of a clamped isotropic square plate. Furthermore, to verify the thermomechanical results, the temperature field of an FGM composite beam is compared with the previous data. Then we analyze the thermal buckling behavior of clamped square Al_2O_3–Ni FGM plates under time-independent or time-dependent temperature rise across the thickness direction.

A. Isotropic Plates

To demonstrate the present results, the critical temperatures of a clamped isotropic square plate under uniform and linear temperature rise in the x direction are investigated.

The temperature field under uniform temperature rise is expressed as

$$\Delta T = T_0, \qquad T = T_{\text{ref}} + \Delta T = T_{\text{ref}} + T_0 \tag{38}$$

where T_0 indicates the temperature change. The temperature field under linear temperature rise in the x direction is expressed as

$$\Delta T(x) = T_1(x/a), \qquad T(x) = T_{\text{ref}} + \Delta T(x) = T_{\text{ref}} + T_1(x/a) \tag{39}$$

where T_1 denotes the temperature gradient.

The critical temperature changes of each work, $T_{0\,\text{cr}}$ and $T_{1\,\text{cr}}$, are presented in Table 1. It shows that the present data compare well with analytic results[16] and FEM results using semiloof elements.[17]

B. FGM Composite Beams

To demonstrate the thermomechanical results, we analyze the thermal behavior of a symmetric two-dimensional functionally graded composite beam, composed of ceramic (Al_2O_3)–FGM–metal (Ni).[7] In the FGM layer, material properties are assumed to be varied continuously in the thickness direction only and properties for Al_2O_3 and Ni are listed in Table 2. At the bottom surface of the beam, a room temperature T_{ref} of 290 K is maintained, while on the top surface a heating temperature $f(t)$ is applied as follows:

$$0 \le t \le 3, \qquad f(t) = T_{\text{ref}} + T_3(t/3)$$
$$t \ge 3, \qquad f(t) = T_{\text{ref}} + T_3 \tag{40}$$

In this study, 1000 K is used for T_3, and the thickness ratios of ceramic, FGM, and metal layers are 0.4, 0.2, and 0.4, respectively.[7] Figure 2 represents the temperature–time histories at the interface between ceramic and FGM layers for an FGM composite beam.

Table 1 Critical temperature change of a clamped isotropic square plate under uniform or linear temperature distribution[a]

	Source		
Temperature rise	Analytic[16]	FEM[17]	Present
Uniform	168.71	167.70	167.73
Linearly varying in x direction	337.42	332.50	330.27

[a] $a/h = 100$, $v = 0.3$, $\alpha = 2 \times 10^{-6}$.

Table 2 Material properties of Al_2O_3 and Ni (Ref. 7)

	Constituents	
Property	Al_2O_3	Ni
Young's modulus, GPa	393.0	199.5
Poisson's ratio	0.25	0.30
Density, kg/m^3	3970	8900
Specific heat, J/kg · K	775	444
Thermal conductivity, W/m · K	30.1	90.7
Thermal expansion coefficient, °C × 10^{-6}	8.8	13.3

Table 3 Critical temperature change with respect to volume fraction index and geometric parameters under uniform temperature rise

	a/h ($a/b = 1$)		
n	20	50	100
0.3	671.52	112.15	28.21
1	729.67	121.53	30.56
5	818.27	135.93	34.17

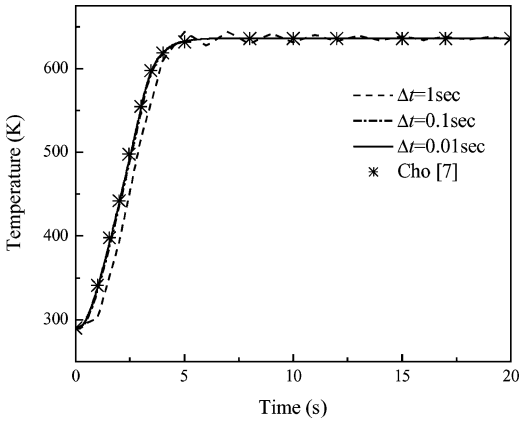

Fig. 2 Temperature–time histories at the ceramic–FGM layer interface of an FGM composite beam ($a/b = 1$, $a/h = 10$, $n = 0.3$).

The time increment Δt of 0.1 was used in previous work.[7] This figure shows that the present results compare very well with those of previous work. It also shows that, when $\Delta t \le 0.1$ s, the temperature–time responses are much the same.

C. FGM Plates

In this section, we analyze the thermal buckling of clamped square Al_2O_3–Ni FGM plates under time-independent or time-dependent temperature rise through the thickness direction. The thermal buckling behavior under time-dependent temperature rise is compared with that under time-independent temperature rise. In time-independent temperature distribution, thermal buckling under uniform, linear, and sinusoidal temperature rise are investigated. The temperature fields under time-independent temperature rise are given in Appendix B. Material properties are varied continuously in the thickness direction only and the reference temperature T_{ref} is assumed to be 290 K.

1. Time-Independent Temperature Rise

a. Uniform temperature rise. Table 3 represents the critical temperature change with respect to volume fraction index and a/h under uniform temperature rise. This shows that the critical temperature change increases as volume fraction index n is increased. This is because, for FGMs, as the volume fraction index is increased, the contained quantity of ceramic increases. However, when the geometric parameter a/h is increased, the critical temperature change decreases. It shows that, with increasing plate thickness, the critical temperature change becomes higher.

Figure 3 describes the variation of critical temperature change with a/h and volume fraction index under uniform temperature rise. The isotropic Al_2O_3 and Ni cases correspond to all-ceramic plates and all-metal plates, respectively, whereas the other cases, $n = 0.3$, 1, and 5, are for the FGM plates with two constituent materials. The critical temperature change of FGM plates is higher than that of the all-metal plates but lower than that of the all-ceramic plates. In addition, the critical temperature change increases as volume fraction index n is increased. However, in all material cases, the critical temperature change decreases rapidly when the geometric parameter a/h is increased.

b. Linear temperature rise. The critical temperature gradient with respect to volume fraction index and a/h under linear

Table 4 Critical temperature gradient with respect to volume fraction index and geometric parameters under linear temperature rise

	a/h ($a/h=1$)		
n	20	50	100
0.3	1301.62	217.17	54.63
1	1418.25	235.89	59.31
5	1622.81	269.36	67.70

Table 5 Critical temperature gradient with respect to volume fraction index and geometric parameters under sinusoidal temperature rise

	a/h ($a/h=1$)		
n	20	50	100
0.3	1763.04	294.42	74.07
1	1931.68	321.50	80.84
5	2229.33	370.38	93.11

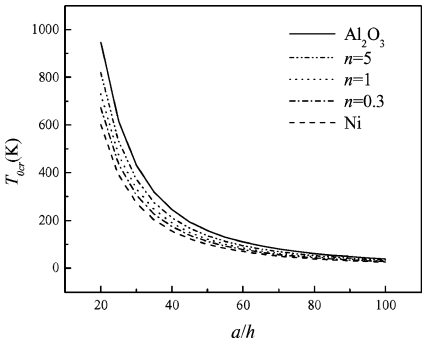

Fig. 3 Variation of critical temperature change with *a/h* under uniform temperature rise.

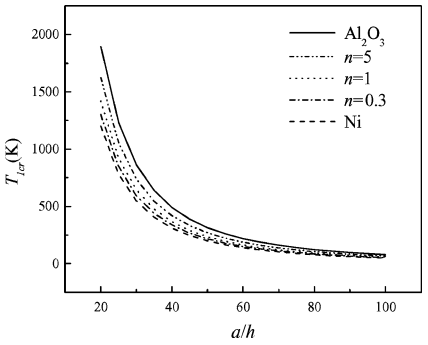

Fig. 4 Variation of critical temperature gradient with *a/h* under linear temperature rise.

temperature rise is presented in Table 4. The critical temperature gradient increases as volume fraction index n is increased or a/h is decreased.

Figure 4 describes the variation of critical temperature gradient with a/h and volume fraction index under linear temperature rise. The critical temperature gradient of FGM plates is higher than that of the all-metal plates but lower than that of the all-ceramic plates. Furthermore, the critical temperature gradient increases as volume fraction index n is increased. However, it decreases when the geometric parameter a/h is increased. These responses are very similar to those under uniform temperature rise, but the critical temperature gradient under linear temperature rise is higher than that under uniform temperature rise.

c. Sinusoidal temperature rise. Table 5 represents the critical temperature gradient according to volume fraction index and a/h under sinusoidal temperature rise. The critical temperature gradient increases as volume fraction index n is increased; however, it decreases as the geometric parameter a/h is increased. Figure 5 describes the variation of critical temperature gradient with a/h and volume fraction index under sinusoidal temperature rise. The critical temperature gradient of FGM plates is higher than that of the all-metal plates but lower than that of the all-ceramic plates. In addition, the critical temperature gradient increases as volume fraction index n is increased or a/h is decreased. These results are very similar to those under uniform and linear temperature rise, but the critical temperature gradient under sinusoidal temperature rise is higher than that under linear temperature rise, which is higher than that under uniform temperature rise.

Table 6 Critical temperature gradient according to the time increment and volume fraction index when the time is 5 s[a]

	Δt, s			
n	0.5	0.1	0.05	0.01
0.3	237.79	237.57	237.54	237.51
1	288.69	288.29	288.21	288.13
5	316.54	315.87	315.73	315.61

[a] $a/b=1$, $a/h=50$.

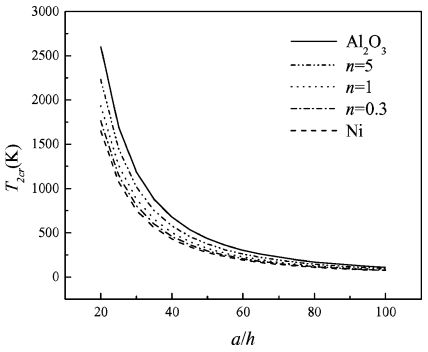

Fig. 5 Variation of critical temperature gradient with *a/h* under sinusoidal temperature rise.

2. Time-Dependent Temperature Rise

In this part, we analyze the thermomechanical buckling behavior of clamped square Al_2O_3–Ni FGM plates. At the bottom surface of the plate, a room temperature T_{ref} of 290 K is maintained while, on the top surface, a heating temperature of Eq. (40) is applied. The temperature field under time-dependent temperature rise across the thickness direction is obtained by solving Eqs. (11) and (14). In element levels, the temperature rise ΔT is expressed as

$$\Delta T = \boldsymbol{N}\boldsymbol{T}_e - T_{\text{ref}} \tag{41}$$

where $\boldsymbol{T}_e$ denotes the element nodal temperatures. From Eqs. (41) and (2), Eq. (17) can be expressed as

$$\boldsymbol{E}^0 = \left[\alpha_c + (\alpha_m - \alpha_c)(1 - z/h)^n\right](\boldsymbol{N}\boldsymbol{T}_e - T_{\text{ref}})[1 \quad 1 \quad 1 \quad 0 \quad 0 \quad 0]^T \tag{42}$$

The critical temperature gradient $T_{3\,\text{cr}}$ can be obtained by solving Eq. (33).

To select the pertinent value of time increment, Δt, the critical temperature gradient according to the time increment and volume fraction index is analyzed, as presented in Table 6. When the time increment is decreased, the critical temperature gradient decreases slowly. The differences of the critical temperature gradient become very small when $\Delta t \leq 0.1$ s. Thus, to save computing time without sacrificing accuracy, the time increment of 0.1 s is adopted in the following analyses.

Figure 6 describes the thermal buckling mode shape of a clamped square Al_2O_3–Ni FGM plate under time-dependent temperature rise when the time is 3 s. The three-dimensional mode shape is shown

Table 7 Critical temperature gradient with respect to volume fraction index and geometric parameters when the time is 3 s

	a/h $(a/b=1)$		
n	20	50	100
0.3	1680.75	280.64	70.60
1	2111.27	351.54	88.40
5	2376.63	394.97	99.29

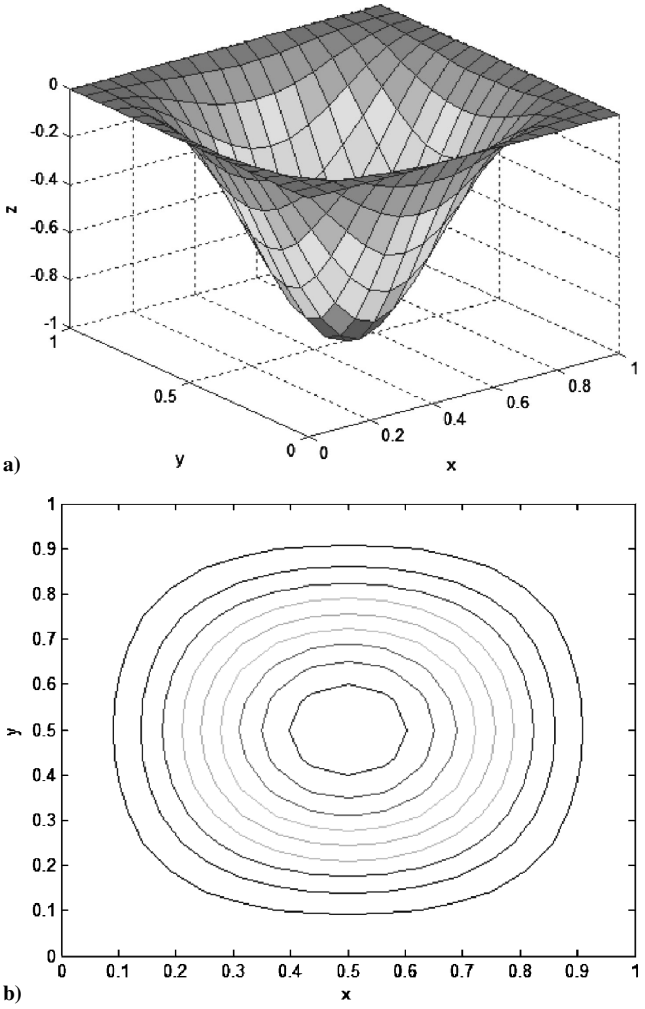

Fig. 6 Thermal buckling mode shape of an Al_2O_3–Ni FGM plate ($a/b=1$, $a/h=50$, $n=0.3$).

in Fig. 6a and the contour in Fig. 6b. In this case, the (1,1) mode shape is presented and the critical temperature is 570.64 K.

The time histories of the critical temperature gradient are presented in Fig. 7. When the volume fraction index n is increased, the critical temperature gradient increases. The critical temperature gradient decreases rapidly with increase of time when time is than 5 s. However, the decrease of critical temperature gradient becomes very small and converges as time is increased when time is longer than 5 s. This is because the heating temperature is constant after 3 s. As a result, when the time is increased, the overall temperature of the structure increases; thus, the critical temperature decreases.

Tables 7–9 represent the critical temperature gradient with respect to volume fraction index and a/h under time-dependent temperature rise when the time is 3, 5, and 15 s, respectively. The critical temperature gradient increases as volume fraction index n is increased; however, it decreases as the geometric parameter a/h is increased. Figure 8 shows the variation of critical temperature gradient with a/h and volume fraction index under time-dependent temperature

Table 8 Critical temperature gradient with respect to volume fraction index and geometric parameters when the time is 5 s

	a/h $(a/b=1)$		
n	20	50	100
0.3	1423.53	237.57	59.76
1	1732.42	288.29	72.49
5	1902.24	315.87	79.40

Table 9 Critical temperature gradient with respect to volume fraction index and geometric parameters when the time is 15 s

	a/h $(a/b=1)$		
n	20	50	100
0.3	1417.91	236.63	59.53
1	1715.61	285.48	71.78
5	1872.00	310.83	78.13

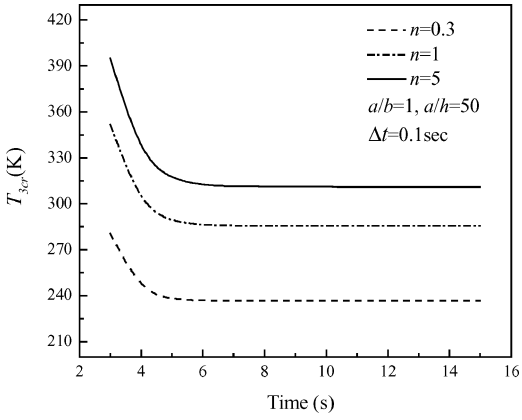

Fig. 7 Time histories of the critical temperature gradient.

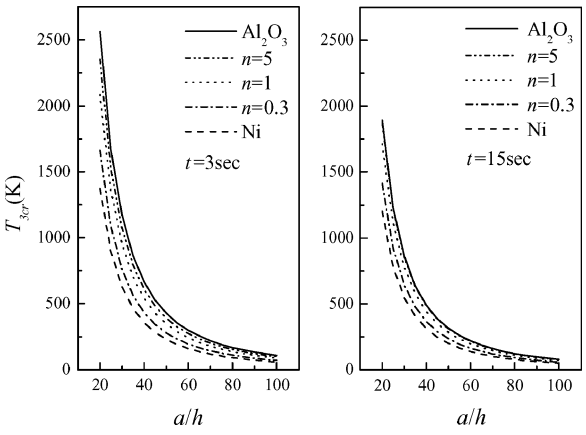

Fig. 8 Variation of critical temperature gradient with a/h when the time $t=3$ and 15 s.

rise when the time is 3 and 15 s. The critical temperature gradient of FGM plates is higher than that of the all-metal plates but lower than that of the all-ceramic plates. In addition, the critical temperature gradient increases as volume fraction index n is increased or a/h is decreased. These responses are very similar to those under time-independent temperature rise. One can also find that the critical temperature gradient when the time is 3 s is higher than that when the time is 15 s.

Comparing the results shows the critical temperature gradient under time-dependent temperature rise to be higher than that under linear temperature rise but lower than that under sinusoidal

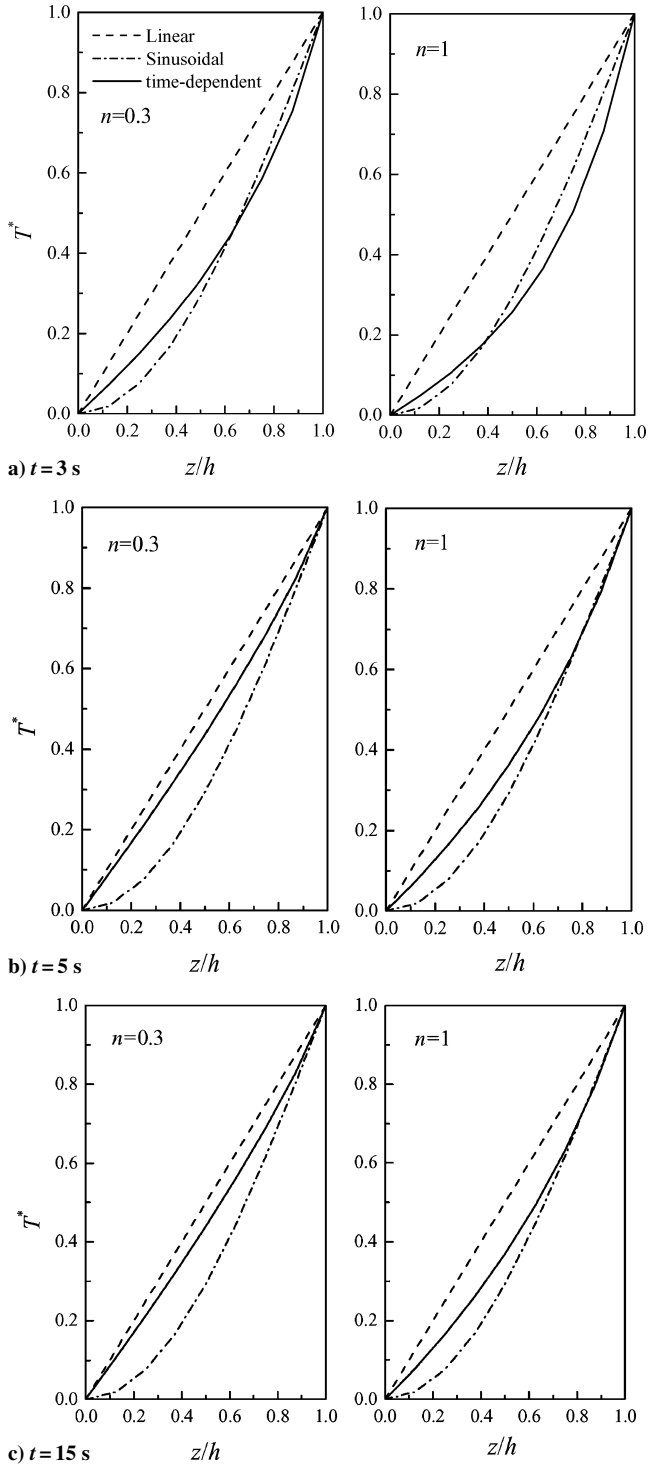

Fig. 9 Temperature distributions in the thickness direction ($a/h = 50$).

temperature rise when the time is 5 or 15 s. However, when the time is 3 s, the responses are different according to the volume fraction index. When volume fraction index n is 0.3, the responses are same as those when time is 5 or 15 s. However, in the case of $n = 1$ or 5, the critical temperature gradients are higher than those under sinusoidal temperature rise. This trend can be investigated by comparing the temperature fields in Fig. 9. In this figure, T^* indicates the normalized temperature. The overall temperature of the structure becomes higher when time is increased or volume fraction index n is decreased. This is because, as n is increased, the contained quantity of ceramic increases. In Fig. 9a, the overall temperature of the structure under time-dependent temperature rise is the smallest when n and time are 1 and 3 s, respectively. Thus, the critical temperature gradient under time-dependent temperature rise is the largest in this case. However, except for this case, the overall temperature of the structure under time-dependent temperature rise is higher than that under sinusoidal temperature rise but lower than that under linear temperature rise in Fig. 9. Therefore, the critical temperature gradient under time-dependent temperature rise is higher than that under linear temperature rise but lower than that under sinusoidal temperature rise. From the result, the critical temperature gradient under time-dependent temperature rise is between that under linear and sinusoidal temperature rise as time is increased.

V. Conclusions

The three-dimensional thermomechanical buckling analysis of FGMs is investigated using the finite element method. To check the validity of the present data, the critical temperatures of isotropic plates and the temperature field of Al_2O_3–Ni FGM composite beams are compared with previous works. The present results agree well with those of previous studies. The thermomechanical buckling behavior of clamped Al_2O_3–Ni FGM plates under time-dependent temperature rise are compared with that under time-independent temperature rise. In the case of time-independent temperature distribution, the temperature field is assumed to be uniform, linear, and sinusoidal through the thickness direction. The critical temperature gradient increases when volume fraction index is increased; however, it decreases rapidly when a/h is increased. The critical temperature gradient under sinusoidal temperature rise is higher than that under linear temperature rise, which is higher than that under uniform temperature rise. In the case of time-dependent temperature distribution, the critical temperature gradient decreases when time is increased; it also decreases as volume fraction index is decreased or a/h is increased. Comparing the results under time-dependent temperature rise to those under time-independent temperature rise, as time is increased, shows that the overall temperature of the structure under time-dependent temperature rise is higher than that under sinusoidal temperature rise but lower than that under linear temperature rise. Therefore, the critical temperature gradient under time-dependent temperature rise is higher than that under linear temperature rise but lower than that under sinusoidal temperature rise.

Appendix A: Assumed Strain Polynomial Matrix

The assumed strain field of an 18-node solid element is assumed to be the 50β version follows as[14]:

$$[E_{xx} \quad E_{yy} \quad E_{zz} \quad E_{xy} \quad E_{yz} \quad E_{zx}]^T = \boldsymbol{P}\boldsymbol{\beta}$$

$$E_{xx} = \beta_1 + \xi\beta_2 + \eta\beta_3 + \xi\eta\beta_4 + \zeta(\beta_{25} + \xi\beta_{26} + \eta\beta_{27} + \xi\eta\beta_{28}) + \xi\eta^2(\beta_{45} + \zeta\beta_{48})$$

$$E_{yy} = \beta_5 + \xi\beta_6 + \eta\beta_7 + \xi\eta\beta_8 + \zeta(\beta_{29} + \xi\beta_{30} + \eta\beta_{31} + \xi\eta\beta_{32}) + \xi^2\eta(\beta_{46} + \zeta\beta_{49})$$

$$E_{zz} = \beta_9 + \xi\beta_{10} + \eta\beta_{11} + \xi\eta\beta_{12}$$

$$E_{xy} = \beta_{13} + \xi\beta_{14} + \eta\beta_{15} + \xi\eta\beta_{16} + \zeta(\beta_{33} + \xi\beta_{34} + \eta\beta_{35} + \xi\eta\beta_{36})$$

$$E_{yz} = \beta_{17} + \xi\beta_{18} + \eta\beta_{19} + \xi\eta\beta_{20} + \zeta(\beta_{37} + \xi\beta_{38} + \eta\beta_{39} + \xi\eta\beta_{40}) + \xi^2\eta(\beta_{47} + \zeta\beta_{50})$$

$$E_{zx} = \beta_{21} + \xi\beta_{22} + \eta\beta_{23} + \xi\eta\beta_{24} + \zeta(\beta_{41} + \xi\beta_{42} + \eta\beta_{43} + \xi\eta\beta_{44}) + \xi\eta^2(\beta_{47} + \zeta\beta_{50}) \tag{A1}$$

Appendix B: Temperature Field Under Time-Independent Temperature Rise

The temperature field under uniform temperature rise is expressed as Eq. (38), and from Eqs. (2) and (38), Eq. (17) can be expressed as follows:

$$\boldsymbol{E}^0 = [\alpha(z)T_0 \quad \alpha(z)T_0 \quad \alpha(z)T_0 \quad 0 \quad 0 \quad 0]^T = [\alpha_c + (\alpha_m - \alpha_c)(1 - z/h)^n]T_0[1 \quad 1 \quad 1 \quad 0 \quad 0 \quad 0]^T \tag{B1}$$

The critical temperature change $T_{0\,\mathrm{cr}}$ can be obtained by solving Eq. (33).

The temperature field under linear temperature rise across the thickness direction is assumed to be

$$\Delta T(z) = T_1(z/h), \qquad T(z) = T_{\mathrm{ref}} + \Delta T(z) = T_{\mathrm{ref}} + T_1(z/h) \tag{B2}$$

where T_1 denotes the temperature gradient. From Eqs. (2) and (B2), Eq. (17) can be expressed as follows:

$$\boldsymbol{E}^0 = \left[\alpha_c + (\alpha_m - \alpha_c)(1 - z/h)^n\right] T_1(z/h)[1 \quad 1 \quad 1 \quad 0 \quad 0 \quad 0]^T \tag{B3}$$

The critical temperature gradient $T_{1\,\mathrm{cr}}$ can be obtained by solving Eq. (33).

The temperature field under sinusoidal temperature rise through the thickness direction is assumed to be

$$\Delta T(z) = T_2\{1 - \cos[(\pi/2)(z/h)]\}$$

$$T(z) = T_{\mathrm{ref}} + \Delta T(z) = T_{\mathrm{ref}} + T_2\{1 - \cos[(\pi/2)(z/h)]\} \tag{B4}$$

where T_2 indicates the temperature gradient. From Eqs. (2) and (B4), Eq. (17) can be expressed as follows:

$$\boldsymbol{E}^0 = \left[\alpha_c + (\alpha_m - \alpha_c)(1 - z/h)^n\right] T_2 \times \{1 - \cos[(\pi/2)(z/h)]\}[1 \quad 1 \quad 1 \quad 0 \quad 0 \quad 0]^T \tag{B5}$$

By solving Eq. (33), the critical temperature gradient $T_{2\,\mathrm{cr}}$ can be obtained.

Acknowledgment

This work was supported by the Brain Korea 21 project.

References

[1]Markworth, A. J., Ramesh, K. S., and Parks, W. P., Jr., "Modelling Studies Applied to Functionally Graded Materials," *Journal of Materials Science*, Vol. 30, No. 9, 1995, pp. 2183–2193.

[2]Ravichandran, K. S., "Thermal Residual Stresses in a Functionally Graded Material System," *Materials Science and Engineering A*, Vol. 201, Nos. 1–2, 1995, pp. 269–276.

[3]Fuchiyama, T., and Noda, N., "Analysis of Thermal Stress in a Plate of Functionally Gradient Material," *JSAE Review*, Vol. 16, No. 3, 1995, pp. 263–268.

[4]Reddy, J. N., and Cheng, Z. Q., "Three-Dimensional Thermomechanical Deformations of Functionally Graded Rectangular Plates," *European Journal of Mechanics A: Solids*, Vol. 20, No. 5, 2001, pp. 841–855.

[5]Cheng, Z. Q., and Batra, R. C., "Three-Dimensional Thermoelastic Deformations of a Functionally Graded Elliptic Plate," *Composites B: Engineering*, Vol. 31, No. 2, 2000, pp. 97–106.

[6]Vel, S. S., and Batra, R. C., "Three-Dimensional Analysis of Transient Thermal Stresses in Functionally Graded Plates," *International Journal of Solids and Structures*, Vol. 40, No. 25, 2003, pp. 7181–7196.

[7]Cho, J. R., and Oden, J. T., "Functionally Graded Material: A Parametric Study on Thermal-Stress Characteristics Using the Crank–Nicolson–Galerkin Scheme," *Computer Methods in Applied Mechanics and Engineering*, Vol. 188, Nos. 1–3, 2000, pp. 17–38.

[8]Feldman, E., and Aboudi, J., "Buckling Analysis of Functionally Graded Plates Subjected to Uniaxial Loading," *Composite Structures*, Vol. 38, Nos. 1–4, 1997, pp. 29–36.

[9]Javaheri, R., and Eslami, M. R., "Thermal Buckling of Functionally Graded Plates," *AIAA Journal*, Vol. 40, No. 1, 2002, pp. 162–169.

[10]Najafizadeh, M. M., and Eslami, M. R., "First-Order-Theory-Based Thermoelastic Stability of Functionally Graded Material Circular Plates," *AIAA Journal*, Vol. 40, No. 7, 2002, pp. 1444–1450.

[11]Yang, J., and Shen, H. S., "Nonlinear Bending Analysis of Shear Deformable Functionally Graded Plates Subjected to Thermo-Mechanical Loads Under Various Boundary Conditions," *Composites B: Engineering*, Vol. 34, No. 2, 2003, pp. 103–115.

[12]Lanhe, W., "Thermal Buckling of a Simply Supported Moderately Thick Rectangular FGM Plate," *Composite Structures*, Vol. 64, No. 2, 2004, pp. 211–218.

[13]Na, K. S., and Kim, J. H., "Three-Dimensional Thermal Buckling Analysis of Functionally Graded Materials," *Composites B: Engineering*, Vol. 35, No. 5, 2004, pp. 429–437.

[14]Kim, Y. H., and Lee, S. W., "Finite Element Analysis of Shell Structures with a Solid Element," Dept. of Aerospace Engineering, Internal Rept., Univ. of Maryland, 1988.

[15]Cook, R. D., Malkus, D. S., and Plesha, M. E., *Concepts and Applications of Finite Element Analysis*, 3rd ed., Wiley, New York, 1989.

[16]Gowda, R. M. S., and Pandalai, K. A. V., "Thermal Buckling of Orthotropic Plates," *Studies in Structural Mechanics*, Indian Inst. of Technology, Madras, India, 1970, pp. 9–44.

[17]Thangaratnam, K. R., Palaninathan, and Ramachandran, J., "Thermal Buckling of Composite Laminated Plates," *Computers and Structures*, Vol. 32, No. 5, 1989, pp. 1117–1124.

B. Sankar
Associate Editor